

Comprehensive understanding of heat-induced degradation of triple-cation mixed halide perovskite for a robust solar cell

Jianming Yang, Xianjie Liu, Yuexing Zhang, Xuerong Zheng, Xiaoxiao He, Han Wang, Fangyu Yue, Slawomir Braun, Jinqun Chen, Jianhua Xu, Yanqing Li, Yizheng Jin, Jianxin Tang, Chungang Duan, Mats Fahlman and Qinye Bao

The self-archived postprint version of this journal article is available at Linköping University Institutional Repository (DiVA):

<http://urn.kb.se/resolve?urn=urn:nbn:se:liu:diva-153365>

N.B.: When citing this work, cite the original publication.

Yang, J., Liu, X., Zhang, Y., Zheng, X., He, X., Wang, H., Yue, F., Braun, S., Chen, J., Xu, J., Li, Y., Jin, Y., Tang, J., Duan, C., Fahlman, M., Bao, Q., (2018), Comprehensive understanding of heat-induced degradation of triple-cation mixed halide perovskite for a robust solar cell, *Nano Energy*, 54, 218-226. <https://doi.org/10.1016/j.nanoen.2018.10.011>

Original publication available at:

<https://doi.org/10.1016/j.nanoen.2018.10.011>

Copyright: Elsevier

<http://www.elsevier.com/>



Article type: Full paper

Comprehensive Understanding of Heat-Induced Degradation of Triple-Cation Mixed Halide Perovskite for a Robust Solar Cell

*Jianming Yang, Xianjie Liu, Yuexing Zhang, Xuerong Zheng, Xiaoxiao He, Han Wang, Fangyu Yue, Slawomir Braun, Jinquan Chen, Jianhua Xu, Yanqing Li, Yizheng Jin, Jianxin Tang, Chungang Duan, Mats Fahlman, Qinye Bao**

J. Yang, H. Wang, Prof. F. Yue, Prof. C. Duan, Prof. Q. Bao
Key Laboratory of Polar Materials and Devices, Ministry of Education, East China Normal University, 200241, Shanghai, P.R. China
E-mail: qybao@clpm.ecnu.edu.cn

Prof. C. Duan, Prof. Q. Bao
Collaborative Innovation Center of Extreme Optics, Shanxi University, Taiyuan, Shanxi, 030006, P.R. China

X. Zhang, Prof. Y. Li, Prof. J. Tang
Institute of Functional Nano & Soft Materials, Soochow University, Suzhou 215123, P. R. China

X. He, Prof. J. Chen, Prof. J. Xu
State Key Laboratory of Precision Spectroscopy, Zhongshan Campus, East China Normal University, 200062, Shanghai, P. R. China

Dr. X. Liu, Dr. S. Braun, Prof. Q. Bao, Prof. M. Fahlman
Department of Physics, Chemistry and Biology, IFM, Linköping University SE-58183 Linköping, Sweden

X. Zheng, Prof. Y. Jin
Centre for Chemistry of High-Performance & Novel Materials, State Key Laboratory of Silicon Material, Department of Chemistry, Zhejiang University, 310027, Hangzhou, P. R. China

Keywords: triple-cation mixed halide perovskite, thermal-induced degradation, stability, efficiency, perovskite solar cell

Abstract

The triple-cation mixed halide perovskite $\text{Cs}_{0.05}(\text{MA}_{0.17}\text{FA}_{0.83})_{0.95}\text{Pb}(\text{I}_{0.83}\text{Br}_{0.17})_3$ emerges as one of the most promising candidates for photovoltaics due to superior optoelectronic properties, but the thermal stability is still a major challenge for the viability of perovskite solar cells towards commercialization. Herein, we firstly explore the thermal response of the photovoltaic performances to access device physical changes. It is shown that the efficiency loss originates from decreased charge mobility, increased trap density and generation of PbI_2 charge recombination centers near the interface. In-depth analysis of evolutions in morphology, chemical composition, dynamic and electronic structure of the perovskite layer at the nanometer scales indicates that it is initial dangling bonds and vacancies on the imperfect surfaces decrease the activation energy and cause the perovskite decomposition in a layer-by-layer pathway sequentially from the film surface to bulk. Based on the results, a strategy of surface passivation to improve the thermal stability is demonstrated and discussed. This work for the first time provides insights into the physical and chemical change of such triple-cation perovskite and indicates that more effort should be invested in surface treatment for enhancing perovskite device stability.

Introduction

Solution-processed solar cells based on metal halide perovskites have attracted tremendous interest in the past few years because of high power conversion efficiency (PCE) at a potentially low cost of production. Owing to the excellent optoelectronic properties of perovskites such as large absorption coefficients, long carrier diffusion lengths, ambipolar charge transport and low defect concentrations,^[1-5] the certified PCE is now 23.3%, surpassing that of dye-sensitized and organic photovoltaics (~ 14%) and **is** competitive with the established photovoltaic technologies, e.g. copper indium gallium selenide cells (~ 22.6%) and crystalline silicon cells (~ 26%).^[6] Thanks to low-cost materials and processes, a bottom-up cost model calculates that the perovskite solar cells can emerge as a cost leader in photovoltaic generation,^[7] which makes it an exciting technology for commercialization. However, despite impressively high efficiencies, such as near 100% internal quantum efficiency over its absorption spectrum,^[8] the often short lifetime of devices is a main challenge that limits large-scale commercial application. It is generally known that the hybrid perovskites are sensitive to moisture, oxygen, irradiation and raised temperature,^[9-14] which can cause severe loss in PCE and operating durability of the device. Moisture and oxygen instability can be addressed by optimized encapsulation,^[15,16] but not thermal degradation as the normal solar device operating temperature can reach up to 85 °C, and can easily exceed this temperature if solar radiation concentrators are utilized.^[17] Therefore, thermal-induced degradation is a key issue for the viability of perovskite solar cells. To overcome this limitation, systematic thermal and ageing studies are required to

understand the degradation processes involved. Recent reports have shown that methylammonium lead iodide (MAPbI₃), the most common hybrid perovskite, suffers strong decomposition both in the inorganic and organic compounds under heating, and the final products depend on temperature^[18,19] and atmosphere^[9,20,21]. However, the knowledge of the physical and chemical mechanisms behind the temperature-dependent degradation is still underdeveloped.

The stability is closely bound up with the perovskite structures, where the general formula of the perovskites is ABX₃ including organic cation A, divalent metal B and halide X shown in Figure 1a. The pure MAPbX₃ and FAPbX₃ perovskite compounds are easy to degrade. The modification of Goldschmidt tolerance factor that related with the ionic radii of the constituents has been demonstrated to be an effective strategy to improve the perovskite structural stability.^[22-24] The emerging mixed perovskites employing FA, MA and Cs on the A site, as well as I and Br on the X site obtain an effective tolerance factor close to 1, enabling a black tetragonal photoactive phase that exhibits enhanced thermal stability.^[25] The devices with such triple-cation perovskites achieve a high stabilized PCE of 21.1%, remaining at 18% after 250 h under continuous working conditions.^[25] Such devices can further be improved to retain 95% of the initial efficiency for over 1000 h through interface engineering of charge selective contact.^[26,27] This device lifetime is still far below the benchmark of the market-dominant silicon cells with an efficiency degradation of 0.5% per year that ensures a 25 years long-term stability. Herein, this work aims to develop a deep understanding of

the degradation mechanisms of the triple-cation perovskite $\text{Cs}_{0.05}(\text{MA}_{0.17}\text{FA}_{0.83})_{0.95}\text{Pb}(\text{I}_{0.83}\text{Br}_{0.17})_3$ at elevated temperature (85 °C according to IEC 61646 standard) and probe the response of the device performances in perovskite solar cells to access macroscopic physical device changes. The findings provide insights into the physical and chemical change of such triple-cation perovskite layers and address that more efforts should be invested to enhance its thermal stability for the future device commercialization.

Results and Discussion

Effect of annealed perovskite film on device degradation

We conducted the study using the triple cation perovskite $\text{Cs}_{0.05}(\text{MA}_{0.17}\text{FA}_{0.83})_{0.95}\text{Pb}(\text{I}_{0.83}\text{Br}_{0.17})_3$ and the p-i-n solar cell devices with ITO/PEDOT: PSS/perovskite/PCBM/Ag architecture (Figure 1b). To rule out the possible degradation caused by the upper stacked layers of electron transporting layer and metallic cathode, the heating processes were only applied on semi-finished cells of ITO/PEDOT:PSS/perovskite films. Figure 1c shows the J-V characteristics of the devices with freshly prepared as well as annealed (85 °C) perovskite films for different durations. The pristine devices exhibit a short-circuit current density (J_{sc}) of 22.28 mA cm^{-2} , an open-circuit voltage (V_{oc}) of 0.94 eV, a fill factor (FF) of 0.72, reaching a PCE of 15.06 %. For the annealed perovskite-based samples, 12, 24, and 48 h, respectively, we observe the dramatic degradations in all device parameters: the J_{sc} decreased to 22.02, 20.25, and 18.40 mA cm^{-2} ; the V_{oc} decreased to 0.87, 0.85, and 0.73 V; the FF

decreased to 0.69, 0.67, and 0.62 ; so that the resulting PCE decreased to 13.24%, 11.70%, and 8.37%. Table 1 summarizes the corresponding performance parameters. (J-V curves of over 50 devices were collected and analyzed, displaying the consistent degradation trends in Figure S1).

The external quantum efficiency (EQE) spectra of the devices confirm current loss across nearly the entire absorption range, see Figure 1d. The EQE intensities drop from 90% to 70% for 48 h-annealed perovskite films. The decreased EQE could originate from reduced light absorption or (and) decreased charge transport efficiency of the photoactive layers.^[28,29] To assess the charge carrier transport in the $\text{Cs}_{0.05}(\text{MA}_{0.17}\text{FA}_{0.83})_{0.95}\text{Pb}(\text{I}_{0.83}\text{Br}_{0.17})_3$ layers before and after annealing, hole-only devices with the diode structure of ITO/PEDOT:PSS/perovskite/MoO₃/Ag were fabricated. The dark J-V curves plotted in Figure 1e can be divided into three regimes including linear ohmic current at low bias, trap-filled limited (TFL) current at intermediate voltage and space-charge limited current (SCLC) at high bias where mobile carriers dominate the transport.^[30,31] The abrupt increase in the current and the transition in the applied voltage (V_{TFL}) from the ohmic to TFL behavior are determined from the trap state filled limit. Therefore, the trap density (N_{traps}) can be evaluated according to the following equation:^[30] $N_{\text{traps}} = \frac{2\varepsilon_0\varepsilon_r V_{\text{TFC}}}{eL^2}$, where ε_0 is the vacuum permittivity, ε_r is the dielectric constant of perovskite, L is the thickness of perovskite layer (~600 nm). After 48 h annealing, the trap density in the $\text{Cs}_{0.05}(\text{MA}_{0.17}\text{FA}_{0.83})_{0.95}\text{Pb}(\text{I}_{0.83}\text{Br}_{0.17})_3$ layer was estimated to increase from $1.41 \times$

10^{16} to $2.04 \times 10^{16} \text{ cm}^{-3}$. We also calculated the mobility (μ) of the perovskite layers in the SCLC regime by fitting with the Mott-Gurney law as^[31] $J = \frac{9}{8} \epsilon_r \epsilon_0 \mu \frac{V^2}{L^3}$, where J and V are the current density and the base voltage, respectively. The hole mobility of the pristine perovskite-based samples is extrapolated to be $0.52 \text{ cm}^2 \text{ V}^{-1} \text{ S}^{-1}$, in line with previous reports.^[32] However, the mobility significantly diminishes to $3.90 \times 10^{-2} \text{ cm}^2 \text{ V}^{-1} \text{ S}^{-1}$ after 48 h annealing. From the calculated results we find that the raised temperature increases the trap density and reduces the carrier mobility in the triple cation perovskite films (summarized in Table S1), which contribute to the severe loss of device performance.

Figure 1f presents the Nyquist plots of the impedance spectroscopy in dark condition at close to open circuit voltage. An equivalent circuit consisting of a series resistance (R_S), a charge transfer resistance R_{CT} and a parallel capacitor (C) is depicted in the inset. Since all devices possess the same structure and conductive electrodes, the R_S shows a slight change from 27.79 to 33.35 Ω for the pristine and annealed samples. A major difference is found in R_{CT} , rising from 2.04 to 3.27 k Ω . Larger R_{CT} for the device fabricated by the annealed perovskite films indicates impaired charge transfer not only in the bulk perovskite layer but also likely at the contact with the adjacent layer.^[33]

Morphology

To explore the origin of this elevated temperature effect, Figure 2a-2d display the

evolution of the $\text{Cs}_{0.05}(\text{MA}_{0.17}\text{FA}_{0.83})_{0.95}\text{Pb}(\text{I}_{0.83}\text{Br}_{0.17})_3$ perovskite film surface morphologies during annealing at 85 °C via scanning electron microscopy (SEM). The surface of the fresh perovskite film is uniform and smooth, and the crystal grains and boundaries are well-defined. After 12 h annealing, the crystal grains grow, and larger grain domains with the size of ~ 250 nm were observed (inserted magnified image), suggesting that the moderate annealing promotes regular grain growth by consuming neighboring crystals.^[34] After prolonged annealing from 12 to 48 h, the film becomes uneven and rough. It is evident that many bright needles appear at the grain boundaries and gradually break the perovskite grains, indicating that the triple cation perovskite undergoes a significant degradation under thermal stress. In addition, such thermal induced degradation significantly **reduces** the film surface energies, as the contact angles increase from 33.2° to 70.1°, see Figure **S3**. Conductive atomic force microscopy (c-AFM) is used to study the variation of the surface conductivity upon annealing. As can be seen from the current mapping in figure 2e and 2f, the overall conductivity of the film distinctly decreases, especially in the regions where the grainy features correspondingly appear in the topography image (see Figure **S4**) upon degradation (high-contrast dark areas signify minimal contribution to the electric current).

Figure 2g and 2h depict the cross-sectional SEM images of solar cells based on pristine and degraded perovskite films annealed for 48 h. In the pristine case, the stacked multilayers are neat and tight, whereas the detachment of the perovskite layer from the underlying PEDOT:PSS layer is observed for the degraded sample, as

previously reported by Han et.al.^[35]. The delamination behavior conceivably would restrict the charge transfer between perovskite and PEDOT:PSS, and thus decrease the device current during operation. Next, we replaced PEDOT:PSS with SnO₂ since metal oxides are believed to more robust charge transport materials widely applied in recent research.^[36,37] The detachment at the contact interface shows no substrate dependence, see Figure S6, indicating that the observed delamination behavior is intrinsic, resulting from the thermal degradation of the perovskite film itself.

Crystal structure and dynamics

We now turn to structure analysis using x-ray diffraction (XRD) to provide further insight into the device degradation, as shown in Figure 3a. We note that an additional small peak at 12.8° emerges upon thermal stress, representing the partial Cs_{0.05}(MA_{0.17}FA_{0.83})_{0.95}Pb(I_{0.83}Br_{0.17})₃ decomposition into cubic PbI₂ (PDF 073-1753), and the intensity of this peak increases with increased annealing time. The corresponding optical absorption spectra of the annealed perovskite films shows no obvious change with a feature at around 510 nm in Figure 3b. The negligible change is attributed to that only a small volume fraction of PbI₂ is generated (compared to the entire perovskite film) and the absorption feature of PbI₂ overlaps with the perovskite film features (Figure S7). The steady-state photoluminescence (PL), however, shows a clear drop in emission peak intensity with increased annealing time, see Figure 3c. Exciton quenching at the band gap is usually caused by trap-assisted nonradiative recombination.^[38,39] Compared to XRD and absorption measurements, PL detection is

more surface sensitive since the excitation light we use is 465 nm,^[40] which has a penetration depth of tens of nanometers, much less than the thickness of the perovskite film. The PL results hence indicate that the PbI₂ acting as trap states mostly are located close to the film top surface and along the grain boundaries, which is consistent with the morphology images in Figure 2. In addition, for the 48 h annealed perovskite films, a weak red-shifted emission from 766 to 770 nm was observed, which is assigned to the spontaneous radiative recombination between PbI₂ trap states.

The charge carrier dynamics of the thermally degraded triple cation perovskite films were studied by time-resolved PL. The PL lifetimes can be obtained by fitting the decay curves with a biexponential decay function, composing of a fast decay component (τ_1) and a slow decay component (τ_2). τ_1 represents a surface component, especially the non-radiative recombination at the defect sites while τ_2 stands for the direct band-to-band recombination in the bulk perovskite film.^[3,41] The values of the parameters are summarized in Table S2. It is found that the fast decay lifetime τ_1 continually decreases from 30.95 ns for the pristine film to 19.65, 7.87 and 7.05 ns for the degraded films annealed for 12, 24 and 48 h, respectively. The reduced lifetimes indicate an increased number of deep-level trap states emerging on the surface of perovskite films upon annealing, which agrees with the disintegration of the perovskites into PbI₂ defects residues on the surface. Furthermore, the slow decay lifetime τ_2 exhibits an anomalous rise from 128.64 ns for the pristine film to 156.2 ns for the film annealed for 12 h, then it drops down to 94.5 and 83.38 ns for 24 and 48 h annealing,

respectively. We attribute this increased τ_2 lifetime dominating for the short annealing time to a longer carrier diffusion length obtained from the enlarged crystal grains (see Figure 2b),^[42] and the decreased τ_2 lifetime dominating in long-time annealing is attributed to an increased bulk defect density. The diminished τ_1 and τ_2 lifetimes in the final phase together with the electrical measurements in the previous session reveal the decreased charge transport ability in the annealed triple cation perovskite films, which contribute to the degradation of the device performance.

X-ray core level photoelectron (XPS) spectra were collected to examine the chemical composition of the perovskite films as a function of annealing time. The organic A-site component of the perovskite films is evaluated by the N 1s and C 1s spectra in Figure 3e and 3f. The N 1s spectra are fitted with two contributions that represent the N bond in MA (MA-N) and FA (FA-N), at 402.9 and 400.8 eV, respectively. The N atomic ratio of two N components is estimated to be 17:83, which is consistent with the perovskite's expected chemical stoichiometry. Upon annealing for different time periods, the intensity of the MA-N peak gradually attenuates and nearly disappears after 48 h, while the FA-N peak remains constant. The similar behavior is also observed in the C 1s spectra. The intensity of the MA-C peak at 287.0 eV decreases, whereas there is no obvious change in the FA-C peak at 288.6 eV. The third C peak located at low binding energy of 285.2 eV originates from ex-situ absorbed hydrocarbon contamination and the formation of C-H complexes.^[43] These results suggest that the MA component is unstable at 85 °C and decomposes into the gaseous product of NH₃

as well as desorbs from the film surface.^[43] The relative robustness of FA component is further confirmed by FTIR where the C=N stretching vibration at 1710 cm^{-1} remains after heating (Figure S9). The Cs component is also not affected (Figure S8). The inorganic B-site component is determined by Pb 4f core level spectra, shown in Figure 3g. The Pb 4f shows sharp doublet peaks located at 138.7 eV (Pb 4f_{7/2}) and 143.6 eV (Pb 4f_{5/2}), respectively, which can be assigned to the chemical state of Pb²⁺. There is no distinct difference before and after annealing as the vacancy and local chemical environment for lead in perovskite and PbI₂ are virtually the same. The halogen X-site component is evaluated by I 3d core level spectra. It is noted that the intensity of I 3d_{3/2} peak shrinks by approximately 17% after 48 h annealing, accompanying with the MA decomposition. The loss value of 17% is very close to the MA content (16.15%) in the perovskite film, indicating the disappear of MA and I as the ratio of 1:1. For the other halide Br, the peak intensity is stable (Figure S8), because Br possess larger electronegativity than I, the stronger Pb-Br bond is not easily broken under such thermal stress. We thereby could find that the Pb-based inorganic component disintegrates to form PbI₂ (Figure 4a) and HI, and the latter gas escapes from the film surface together with the release of the MA.

Electronic Structure

To achieve a more in-depth understanding of the degradation mechanism, the evolution of electronic structures of the perovskite film under annealing are monitored by ultraviolet photoelectron spectroscopy (UPS) measurement. Particularly relevant

energetics parameters are the work function (WF), the ionization potential (IP), and the energy difference between the valence band maximum (VBM) and the Fermi level (E_F), which govern the charge extraction at contacts. Figure 4a shows UPS spectra of the triple cation perovskite films upon prolonged annealing. The left panel displays the secondary electron cutoff (SECO) used to derive the WF, and the right panel highlights the valence band region referenced to the E_F at zero binding energy. The bottom spectrum corresponds to the pristine perovskite film. The WF and VBM position below E_F are estimated to be 4.6 and 1.31 eV, respectively. The IP defined as the energy difference between vacuum level (VL) and the VBM is thus approximately 5.91 eV. When increasing annealing time from 12 to 48 h, the WF gradually decreases to 4.34 eV, simultaneously, the VBM relative to the E_F shifts towards to higher binding energy by 0.26 eV, resulting in a nearly constant IP. According to the corresponding UPS-derived energy level diagram drawn in Figure 4b, the hole extraction barrier increases as the E_F shifts closer to the conduction band edge, which will result in energy loss of the device.

Discussion

The proposed degradation procedure and mechanism of the triple cation perovskite at 85 °C annealing are schematically summarized in Figure 5. $\text{Cs}_{0.05}(\text{MA}_{0.17}\text{FA}_{0.83})_{0.95}\text{Pb}(\text{I}_{0.83}\text{Br}_{0.17})_3$ can be regarded as the two compounds of $(\text{MAPbI}_3)_{0.1615}$ and $\text{Cs}_{0.05}\text{FA}_{0.7885}\text{Pb}_{0.8385}\text{I}_{2.0055}\text{Br}_{0.51}$. Based on our results, $(\text{MAPbI}_3)_{0.1615}$ undergoes decomposition at 85 °C annealing in the following reaction:

$\text{MAPbI}_3 \rightarrow (-\text{CH}_2-) + \text{NH}_3 (\text{g}) + \text{HI} (\text{g}) + \text{PbI}_2$, where the $(-\text{CH}_2-)$ represents the residual hydrocarbon complex associated to the C1s peak at 285.2 eV that shows increased intensity with increased annealing time (Figure 4f). In contrast, $\text{Cs}_{0.05}\text{FA}_{0.7885}\text{Pb}_{0.8385}\text{I}_{2.0055}\text{Br}_{0.51}$ remains relatively stable under such thermal stress. We propose that the observed degradation hence occurs sequentially in a layer-by-layer fashion from the film surface into the bulk, see Figure 5, because the surface of the solution-processed perovskite film has numerous dangling bonds (Pb^{2+} and I) and vacancies along grain boundaries, which make the film surface energetically less stable and thus more favorable for thermal motions to trigger the decomposition. The Pb-I-Pb bonds along the [001] direction break with the lattice transition from tetragonal to trigonal phase associated with PbI_2 .^[44,45] The exposed underlying layer would then serve as the new surface layer as the degradation progress.

The triple cation perovskite film degradation and organic solar cell efficiency are strongly correlated. The diminished V_{oc} , J_{sc} , FF and final PCE all results from the thermal-induced degradation. It is mainly related to the poor charge transport ability that originates from the decreased charge mobility, the increased trap density and the generation of charge recombination centers (PbI_2) near the interface between the perovskite and the top electron transporting layer (Figure 1 and 3). The detachment behavior between the perovskite and the bottom hole transporting layer also limits the photogenerated carrier collection at the contact (Figure 2). In addition, the surface electronic structure of the perovskite film significantly is modified with an increased

hole extraction barrier that leads to energy loss for the solar cell (Figure 4).

From the proposed degradation mechanism and the impact on the device performance it is easy to understand the fundamental factors responsible for the improved device thermal stability. Since the initial dangling bonds (Pb^{2+} and I) and vacancies on the perovskite film triggers the decomposition from the surface, passivating these defects by interface layers featuring considerable orbital overlap and charge transfer is an effective strategy to improve the thermal stability of perovskite layer.^[46-48] We selected two common organic semiconductor molecules, PCBM and ITIC, dissolved in chlorobenzene as anti-solvent and dripped onto the perovskite films to passivate the defects during film fabrication.^[49] The same degradation experiment process as Figure 1c was again applied for the semi-finished cells of ITO/PEDOT:PSS/passivated perovskite. Upon annealing for 48 h, see Figure 5b and 5c, the device performance exhibits better stability than the previous devices (depicted in Figure 2a). This is due to fullerene's hydrogen bonding interaction and ITIC's Lewis functional group interaction with the defects, thereby reducing the surface activity, retarding surface degradation and improving the whole stability of the perovskite materials. In other words, the less-defect-dense surface should feature an increased decomposition activation energy. We thus expect the continued development of surface/interface engineering to offer significant potential for enhancing the environmental stabilities of perovskite-based devices.

Conclusion

In summary, we report the physical and chemical degradation of the triple cation perovskite layer $\text{Cs}_{0.05}(\text{MA}_{0.17}\text{FA}_{0.83})_{0.95}\text{Pb}(\text{I}_{0.83}\text{Br}_{0.17})_3$ at a raised temperature of 85 °C, and address the performance response of the perovskite-based solar cells. We find that all device parameter including V_{oc} , J_{sc} , FF and final PCE dramatically diminish, which originates from decreased charge mobility, increased trap density and the generation of PbI_2 charge recombination centers near the interface when annealing the perovskite layers for various durations. We observe a severe film detachment behavior at contact interfaces, also limiting charge carrier collection. In-depth analysis of the morphologies, physical and chemical structures at the nanometer scales indicates that it is the initial dangling bonds and vacancies on the imperfect surfaces that decrease the activation energy^[50,51] and cause the perovskite decomposition in a layer-by-layer pathway sequentially from the film surface to bulk accompanied with a lattice transition from tetragonal to PbI_2 trigonal phase. These defects are mainly blamed for the perovskite structure decomposition. During the thermal-induced degradation process, the organic cation MA^+ and halide anion I^- synchronously release, while Cs^+ , FA^+ and Br^- are unaffected. These findings provide important insights into the thermal stability of the complex multi-ion mixed perovskite systems. Based on these results, we further apply the molecules to passivate the surface defects and the improved thermal stability has been achieved. Therefore, continued research into surface treatments for enhancing perovskite stability is likely an important path towards future device commercialization.

Experimental Section

Perovskite film preparation:

Lead iodide/bromide ($\text{PbI}_2/\text{PbBr}_2$) and cesium iodide (CsI) powers were purchased from TCI. Formamidinium iodide (FAI) and Methylammonium bromide (MABr) were obtained from Xi'an Polymer Light Technology Corp. All materials were used without further purification. The $\text{Cs}_{0.05}(\text{FA}_{0.83}\text{MA}_{0.17})_{0.95}\text{Pb}(\text{I}_{0.83}\text{Br}_{0.17})_3$ films were deposited from a precursor solution containing PbI_2 (1.08 M), PbBr_2 (0.2 4M), FAI (1.08 M), MABr (0.22 M) and CsI (0.066 M) in the anhydrous mixed solvents of N, N-dimethylformamide (DMF) and dimethylsulphoxide (DMSO) with 4:1 (v:v). The precursor solution was spin coated in a two-step program at 1000 and 4000 rpm for 10 and 30 s, respectively. During the second step, 100 μL of chlorobenzene was poured on the spinning films with a pipette and the resulting films are annealed at 100 °C for 60 min. For the passivated samples, 0.4 mg/mL of PCBM (Lumtec), and ITIC (Derthon) are dissolved into chlorobenzene and drop into the perovskite via anti-solvent method. All the solutions and perovskite samples were prepared in N_2 -protected glove box.

Device fabrication and characterization:

The ITO substrates ($20 \Omega \text{ cm}^{-1}$) were cleaned by ultrasonication in detergent, acetone, ethanol, isopropanol and deionized water, respectively, then they were further subjected to UV light exposure for 15 min. The PEDOT:PSS solution (CLEVIOS Al 4083) was spin coated on ITO at 4000 rpm for 30 s and annealed at 140 °C for 10 min in ambient

air. The perovskite layers were spin coated on ITO/PEDOT:PSS. 20 mg/ml and PCBM in chlorobenzene solution was deposited on the top perovskite films at 1500 rpm for 30 s as electron transporting layer. After that, Ag (100 nm) layer was thermally evaporated with a shadow mask at the pressure of 2×10^{-6} Torr. For the SnO₂ based device, the SnO₂ colloid precursor was diluted by ultrapure H₂O to achieve a concentration of 2.67%. The dilute solution was spin coated on ITO substrates at 3000 rpm for 30 s followed by annealed at 150 °C for 30 min in ambient air. The following process is the same as the mentioned above. The current density-voltage (J-V) characteristics of the device cells were performed using a programmable Keithley 2612 source measurement unit under simulated solar light (Oriel model 91160, 100 mW/cm², AM 1.5G). The external quantum efficiency (EQE) spectra were recorded using a photo-modulation spectroscopic setup (Newport monochromator). The illumination intensity of solar simulator was calibrated by a standard Si photodiode detector with known spectral response. Alternating current impedance spectroscopy was measured by precise impedance analyzer (Keithley 2400 Series SourceMeters).

Film characterizations:

Prepared fresh perovskite films were put on a hotplate subjected to 85 °C in N₂ filled glove box, covered by a petri dish and a cap made by aluminum foil to eliminate the effect of light. Controlled samples were kept in the same condition without annealing. Surface morphologies of the fresh and degraded films were obtained by high-resolution SEM (Carl Zeiss, Merlin). The conductive mapping was recorded via c-AFM (Veeco

MultiMode V) using Pt/Ir coated Si tips with a quoted force constant of 0.2 N m^{-1} (Nanosensors, PPP-CONT). The crystallographic properties of the films were measured by XRD with monochromatic Cu K α radiation on analytical apparatus (Empyrean). The optical absorption spectra of the films were measured with Perkin Elmer model Lambda 750 instrument. Steady-state PL measurements were performed using Horiba Jobin-Yvon FL-3 with a 470 nm excitation wavelength. The FTIR spectra were characterized by a Bruker Fourier Transform Infrared Spectrometer. XPS and UPS spectra were obtained via Thermo ESCALAB-250Xi spectrometer system. XPS with a monochromatized Al K α 1486.6 eV was applied to detect elemental constituents and chemical interactions after annealing. The UPS spectra were performed using HeI 21.22 eV as exciting source with energy resolution of 50 meV. Work function was derived from the secondary electron cut-off and the ionization potential from the frontier edge of the occupied density of states. The spectra were calibrated by referencing to the Fermi level of the Ar⁺ ion sputter-clean Au substrate. TRPL spectra were measured by a Time-Correlated Single Photon Counting (TCSPC) system containing a picosecond pulsed diode laser (PDL 800-B, PicoQuant), a stand-alone TCSPC module (PicoHarp 300, PicoQuant) and a single photon counting photomultiplier (PMA165A-N-M, PicoQuant). A monochromator (71SW151, Sofn Instruments) with a slit width of 1 mm was utilized to select the emission wavelength.

Supporting information

Supporting information is available.

Author contributions

Q. B. and J. Y. conceived the research. Y. Z. and Y. Q. performed the conductive atomic force microscopy. X. Z. and Y. J. carried out the photoelectron spectroscopy. X. H., J. C. and J. X. carried out the time-resolved photoluminescence spectroscopy. H. W. and F. Y. carried out Fourier-transform infrared spectroscopy. X. L., S. B., J. T. C.D. and M. F. assisted with data interpretation. J. Y. wrote the first version of the manuscript and all authors participated in manuscript revision and editing.

Acknowledgements

The work is sponsored by the National Science Foundation of China grant (No. 11604099, No. 21875067, No. 51811530011, No. 11474214), the Fundamental Research Funds for the Central Universities, Shanghai Science and Technology Innovation Action Plan (No. 17JC1402500), the Swedish Research Council project grant (2016-05498) and the STINT grant (CH2017-7163). We thank the Open Project of Jiangsu Key Laboratory for Carbon-Based Functional Materials & Device. We also thank Prof. Youshi Chen (East China Normal University) for useful discussion on the degradation.

References

- [1] S. D. Stranks, G. E. Eperon, G. Grancini, C. Menelaou, M. J. Alcocer, T. Leijtens, L. M. Herz, A. Petrozza, H. J. Snaith. *Science*, **2013**, *342*, 341-344.
- [2] G. Xing, N. Mathews, S. Sun, S. S. Lim, Y. M. Lam, M. Gratzel, S. Mhaisalkar, T. C. Sum. *Science*, **2013**, *342*, 344-347.
- [3] D. Shi, V. Adinolfi, R. Comin, M. Yuan, E. Alarousu, A. Buin, Y. Chen, S. Hoogland, A. Rothenberger, K. Katsiev, Y. Losovyj, X. Zhang, P. A. Dowben, O. F. Mohammed, E. H. Sargent, O.

- M. Bakr. *Science*, **2015**, *347*, 519-522.
- [4] W. Rehman, R. L. Milot, G. E. Eperon, C. Wehrenfennig, J. L. Boland, H. J. Snaith, M. B. Johnston, L. M. Herz. *Adv Mater*, **2015**, *27*, 7938-7944.
- [5] Q. Dong, Y. Fang, Y. Shao, P. Mulligan, J. Qiu, L. Cao, J. Huang. *Science*, **2015**, *347*, 967-970.
- [6] S. J. Lee, S. S. Shin, Y. C. Kim, D. Kim, T. K. Ahn, J. H. Noh, J. Seo, S. I. Seok. *J Am Chem Soc*, **2016**, *138*, 3974-3977.
- [7] S. Song, G. Kang, L. Pyeon, C. Lim, G.-Y. Lee, T. Park, J. Choi. *ACS Energy Letters*, **2017**, *2*, 2667-2673.
- [8] B. Yang, O. Dyck, J. Poplawsky, J. Keum, A. Paretzky, S. Das, I. Ivanov, C. Rouleau, G. Duscher, D. Geohegan, K. Xiao. *Journal of the American Chemical Society*, **2015**, *137*, 9210-9213.
- [9] W. Huang, S. Sadhu, S. Ptasinska. *Chemistry of Materials*, **2017**, *29*, 8478-8485.
- [10] N. Aristidou, I. Sanchez-Molina, T. Chotchuangchutchaval, M. Brown, L. Martinez, T. Rath, S. A. Haque. *Angew Chem Int Ed Engl*, **2015**, *54*, 8208-8212.
- [11] R. K. Misra, S. Aharon, B. Li, D. Mogilyansky, I. Visoly-Fisher, L. Etgar, E. A. Katz. *J Phys Chem Lett*, **2015**, *6*, 326-330.
- [12] Y. Li, X. Xu, C. Wang, B. Ecker, J. Yang, J. Huang, Y. Gao. *The Journal of Physical Chemistry C*, **2017**, *121*, 3904-3910.
- [13] T. A. Berhe, W.-N. Su, C.-H. Chen, C.-J. Pan, J.-H. Cheng, H.-M. Chen, M.-C. Tsai, L.-Y. Chen, A. A. Dubale, B.-J. Hwang. *Energy & Environmental Science*, **2016**, *9*, 323-356.
- [14] Q. Fu, X. Tang, B. Huang, T. Hu, L. Tan, L. Chen, Y. Chen. *Advanced Science*, **2018**, 1700387.
- [15] Y. I. Lee, N. J. Jeon, B. J. Kim, H. Shim, T.-Y. Yang, S. I. Seok, J. Seo, S. G. Im. *Advanced Energy Materials*, **2018**, *8*, 1701928.
- [16] F. Matteocci, L. Cinà, E. Lamanna, S. Cacovich, G. Divitini, P. A. Midgley, C. Ducati, A. Di Carlo. *Nano Energy*, **2016**, *30*, 162-172.
- [17] V. Rinnerbauer, A. Lenert, D. M. Bierman, Y. X. Yeng, W. R. Chan, R. D. Geil, J. J. Senkevich, J. D. Joannopoulos, E. N. Wang, M. Soljačić, I. Celanovic. *Advanced Energy Materials*, **2014**, *4*, 1400334.
- [18] B. Brunetti, C. Cavallo, A. Ciccio, G. Gigli, A. Latini. *Sci Rep*, **2016**, *6*, 31896.
- [19] E. J. Juarez-Perez, Z. Hawash, S. R. Raga, L. K. Ono, Y. Qi. *Energy & Environmental Science*, **2016**, *9*, 3406-3410.
- [20] G. Divitini, S. Cacovich, F. Matteocci, L. Cinà, A. Di Carlo, C. Ducati. *Nature Energy*, **2016**, *1*, 15012.
- [21] B. Conings, J. Drikkoningen, N. Gauquelin, A. Babayigit, J. D'Haen, L. D'Olieslaeger, A. Ethirajan, J. Verbeeck, J. Manca, E. Mosconi, F. D. Angelis, H.-G. Boyen. *Advanced Energy Materials*, **2015**, *5*, 1500477.
- [22] V. M. Goldschmidt. *Naturwissenschaften*, **1926**, *14*, 477-485.
- [23] J.-W. Xiao, L. Liu, D. Zhang, N. De Marco, J.-W. Lee, O. Lin, Q. Chen, Y. Yang. *Advanced Energy Materials*, **2017**, *7*, 1700491.
- [24] L. K. Ono, E. J. Juarez-Perez, Y. Qi. *ACS Appl Mater Interfaces*, **2017**, *9*, 30197-30246.
- [25] M. Saliba, T. Matsui, J. Y. Seo, K. Domanski, J. P. Correa-Baena, M. K. Nazeeruddin, S. M. Zakeeruddin, W. Tress, A. Abate, A. Hagfeldt, M. Gratzel. *Energy Environ Sci*, **2016**, *9*, 1989-1997.
- [26] N. Arora, M. I. Dar, A. Hinderhofer, N. Pellet, F. Schreiber, S. M. Zakeeruddin, M. Gratzel. *Science*, **2017**, *358*, 768-771.
- [27] J. A. Christians, P. Schulz, J. S. Tinkham, T. H. Schloemer, S. P. Harvey, B. J. Tremolet de Villers,

- A. Sellinger, J. J. Berry, J. M. Luther. *Nature Energy*, **2018**, *3*, 68-74.
- [28] W. Tress. *Advanced Energy Materials*, **2017**, *7*, 1602358.
- [29] S. Sun, T. Salim, N. Mathews, M. Duchamp, C. Boothroyd, G. Xing, T. C. Sum, Y. M. Lam. *Energy Environ. Sci.*, **2014**, *7*, 399-407.
- [30] R. H. Bube. *Journal of Applied Physics*, **1962**, *33*, 1733-1737.
- [31] A. Rose. *Physical Review*, **1955**, *97*, 1538-1544.
- [32] N. S. Gobalasingham, S. Noh, J. B. Howard, B. C. Thompson. *ACS Appl Mater Interfaces*, **2016**.
- [33] K. Chen, Q. Hu, T. Liu, L. Zhao, D. Luo, J. Wu, Y. Zhang, W. Zhang, F. Liu, T. P. Russell, R. Zhu, Q. Gong. *Adv Mater*, **2016**, *28*, 10718-10724.
- [34] J. Li, Q. Dong, N. Li, L. Wang. *Advanced Energy Materials*, **2017**, *7*, 1602922.
- [35] Y. Han, S. Meyer, Y. Dkhissi, K. Weber, J. M. Pringle, U. Bach, L. Spiccia, Y.-B. Cheng. *Journal of Materials Chemistry A*, **2015**, *3*, 8139-8147.
- [36] Q. Jiang, L. Zhang, H. Wang, X. Yang, J. Meng, H. Liu, Z. Yin, J. Wu, X. Zhang, J. You. *Nature Energy*, **2016**, *2*, 16177.
- [37] J. Xie, K. Huang, X. Yu, Z. Yang, K. Xiao, Y. Qiang, X. Zhu, L. Xu, P. Wang, C. Cui, D. Yang. *ACS Nano*, **2017**, *11*, 9176-9182.
- [38] G. J. Wetzelaer, M. Scheepers, A. M. Sempere, C. Momblona, J. Avila, H. J. Bolink. *Adv Mater*, **2015**, *27*, 1837-1841.
- [39] W. Nie, H. Tsai, J. C. Blancon, F. Liu, C. C. Stoumpos, B. Traore, M. Kepenekian, O. Durand, C. Katan, S. Tretiak, J. Crochet, P. M. Ajayan, M. Kanatzidis, J. Even, A. D. Mohite. *Adv Mater*, **2018**, *30*, 1703879.
- [40] C. Roldán-Carmona, P. Gratia, I. Zimmermann, G. Grancini, P. Gao, M. Graetzel, M. K. Nazeeruddin. *Energy & Environmental Science*, **2015**, *8*, 3550-3556.
- [41] F. Zhang, C. Chen, S. V. Kershaw, C. Xiao, J. Han, B. Zou, X. Wu, S. Chang, Y. Dong, A. L. Rogach, H. Zhong. *ChemNanoMat*, **2017**, *3*, 303-310.
- [42] F. Jiang, Y. Rong, H. Liu, T. Liu, L. Mao, W. Meng, F. Qin, Y. Jiang, B. Luo, S. Xiong, J. Tong, Y. Liu, Z. Li, H. Han, Y. Zhou. *Advanced Functional Materials*, **2016**, *26*, 8119-8127.
- [43] L. Advanced Functional Materials Liu, J. A. McLeod, R. Wang, P. Shen, S. Duhm. *Applied Physics Letters*, **2015**, *107*, 061904.
- [44] F. Brivio, J. M. Frost, J. M. Skelton, A. J. Jackson, O. J. Weber, M. T. Weller, A. R. Goñi, A. M. A. Leguy, P. R. F. Barnes, A. Walsh. *Physical Review B*, **2015**, *92*, 144308.
- [45] Z. Fan, H. Xiao, Y. Wang, Z. Zhao, Z. Lin, H.-C. Cheng, S.-J. Lee, G. Wang, Z. Feng, W. A. Goddard, Y. Huang, X. Duan. *Joule*, **2017**, *1*, 548-562.
- [46] C. Park, H. Ko, D. H. Sin, K. C. Song, K. Cho. *Advanced Functional Materials*, **2017**, *27*, 1703546.
- [47] B. Li, Y. Zhang, L. Fu, T. Yu, S. Zhou, L. Zhang, L. Yin. *Nat Commun*, **2018**, *9*, 1076.
- [48] L. Gao, S. Huang, L. Chen, X. Li, B. Ding, S. Huang, G. Yang. *Solar RRL*, **2018**, 1800088.
- [49] T. Niu, J. Lu, R. Munir, J. Li, D. Barrit, X. Zhang, H. Hu, Z. Yang, A. Amassian, K. Zhao, S. F. Liu. *Adv Mater*, **2018**, *30*, 1706576.
- [50] A. Walsh, D. O. Scanlon, S. Y. Chen, X. G. Gong, S. H. Wei. *Angew. Chem. Int. Edit*, **2015**, *54*, 1791.
- [51] Y. Y. Zhang, S. Y. Chen, P. Xu, H. Xiang, X. G. Gong, A. Walsh, S. H. Wei. *Chinese Phys. Lett.*, **2018**, *35*, 036104.

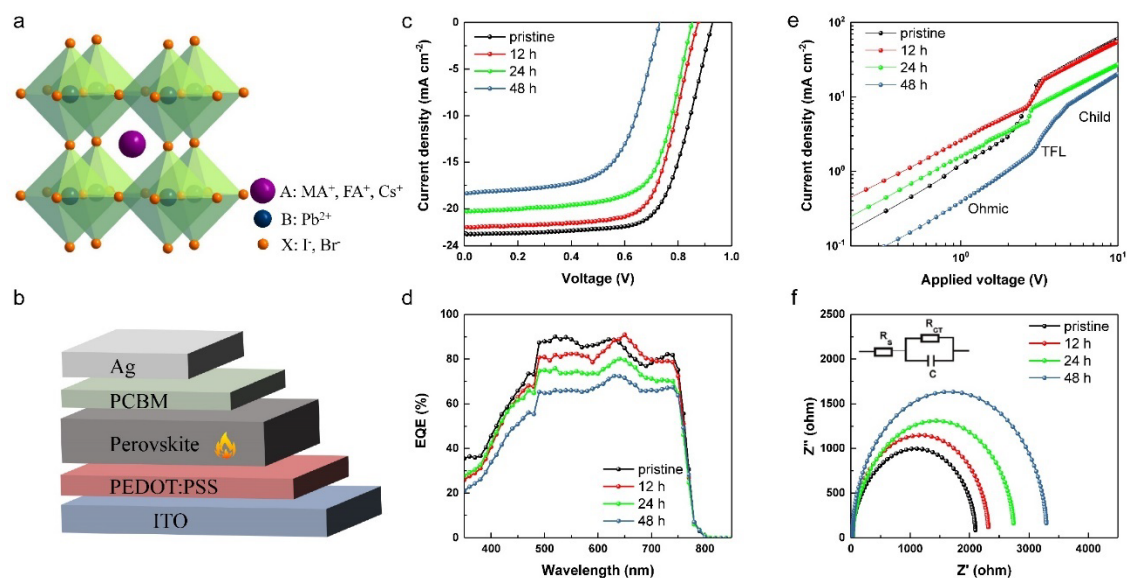


Figure 1. (a) Crystal structure of organic-inorganic hybrid perovskite. (b) The architecture diagram of p-i-n perovskite solar cell devices. Flame icon represents thermal annealing. (c) J-V curves of the devices employing perovskite layers annealed for different duration. (d) EQE spectra. (e) Dark J-V curves of hole-only devices with a structure of ITO/PEDOT:PSS/Perovskite/MoO₃/Ag. (f) Nyquist plots of the impedance spectra. The equivalent circuit is given in the insert.

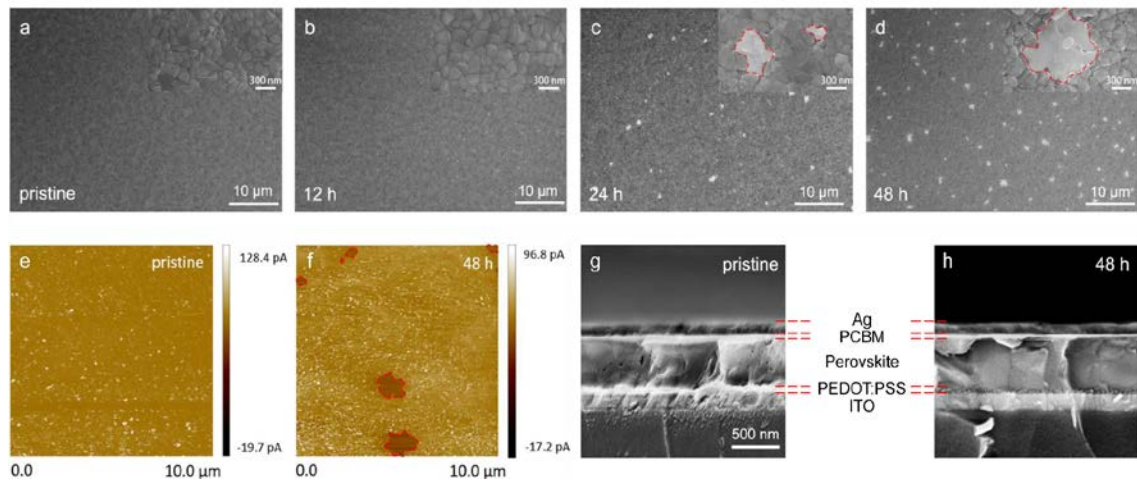


Figure 2. (a-d) Top-view SEM images of the perovskite films with different annealing time. (e, f) C-AFM images of the pristine and annealed perovskite films for 48 h. (g, h) Cross-sectional SEM images of devices employing the pristine and annealed perovskite films for 48 h.

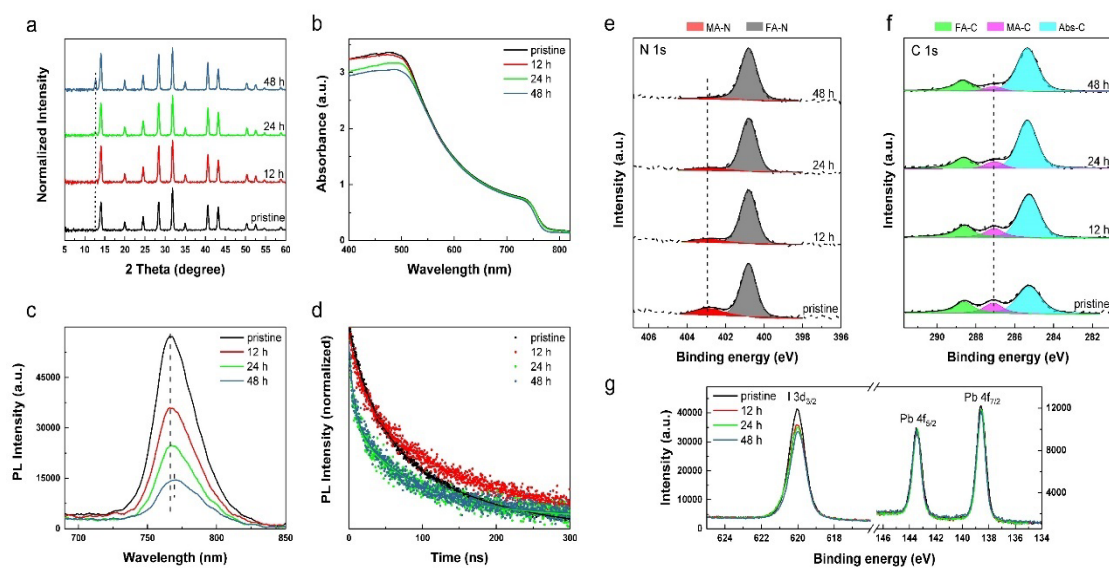


Figure 3. (a) XRD patterns. (b) UV-Vis absorption spectra. (c) Steady-state PL spectra. (d) TRPL spectra. XPS core level spectra of (e) N 1s, (f) Pb 4f and (g) I 3d_{3/2} and Pb 4f of pristine and the annealed perovskite films with different times.

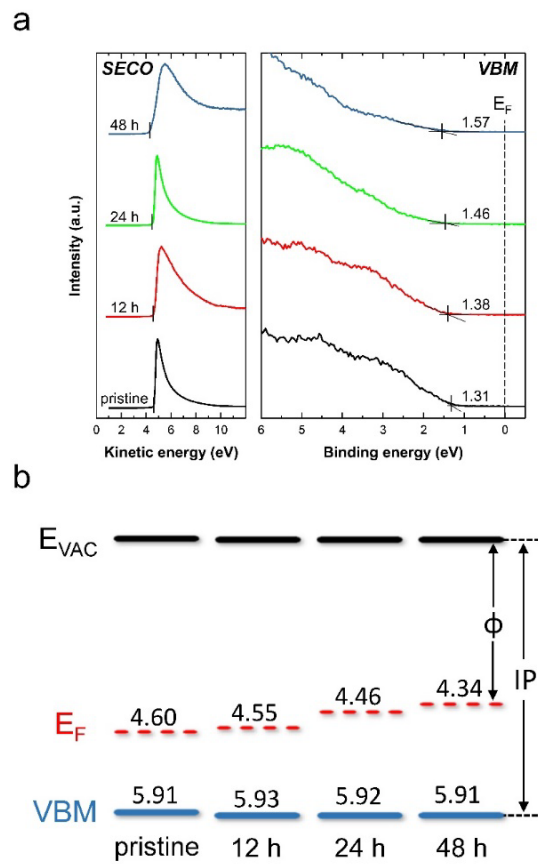


Figure 4. (a) UPS spectra evolution at the secondary electron region and the frontier electronic structure region of the perovskite film as a function of annealing time. (b) Energy-level diagrams of the annealed perovskite films. The Fermi level (E_F) is located at zero binding energy. The SECO and the VBM are shown in the UPS spectra

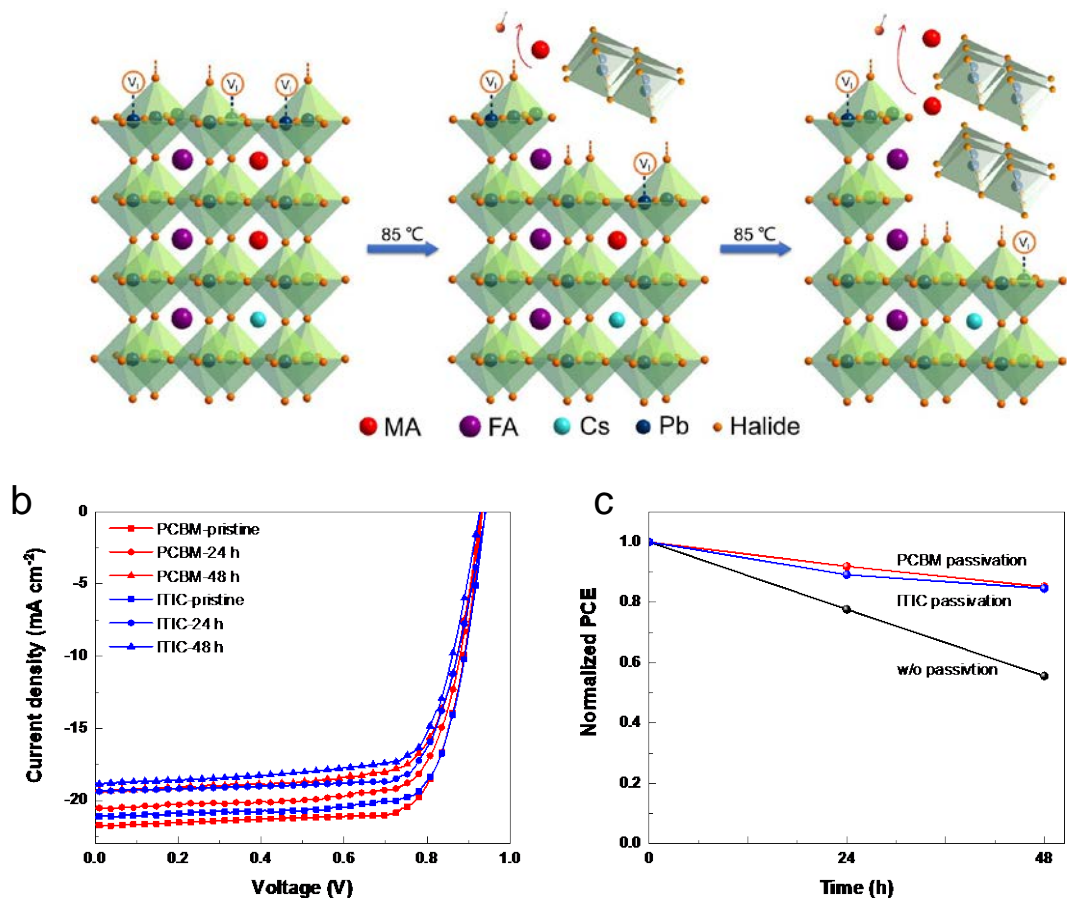


Figure 5. (a) Schematic illustration of the proposed layer-by-layer degradation of the triple cation perovskite $\text{Cs}_{0.05}(\text{MA}_{0.17}\text{FA}_{0.83})_{0.95}\text{Pb}(\text{I}_{0.83}\text{Br}_{0.17})_3$ under 85 °C annealing (b) J-V curves of ITO/PEDOT: PSS/perovskite/PCBM/Ag employing the PCBM and ITIC passivated perovskite layers annealed for different durations. (c) Comparison of efficiency degradation before and after passivation.

Table 1. Performance parameters of perovskite solar cells employing the pristine and annealed perovskite layers.

	J_{sc} (mA cm⁻²)	V_{oc} (V)	FF	PCE
pristine	22.28	0.94	0.72	15.06%
12 h	22.02	0.87	0.69	13.24%
24 h	20.25	0.85	0.67	11.70%
48 h	18.40	0.73	0.62	8.37%

Supporting information

Comprehensive Understanding of Heat-Induced Degradation of Triple-Cation Mixed Halide Perovskite for a Robust Solar Cell

*Jianming Yang, Xianjie Liu, Yuexing Zhang, Xuerong Zheng, Xiaoxiao He, Han Wang, Fangyu Yue, Slawomir Braun, Jinquan Chen, Jianhua Xu, Yanqing Li, Yizheng Jin, Jianxin Tang, Chungang Duan, Mats Fahlman, Qinye Bao**

J. Yang, H. Wang, Prof. F. Yue, Prof. C. Duan, Prof. Q. Bao
Key Laboratory of Polar Materials and Devices, Ministry of Education, East China Normal University, 200241, Shanghai, P.R. China
E-mail: qybao@clpm.ecnu.edu.cn

Prof. C. Duan, Prof. Q. Bao
Collaborative Innovation Center of Extreme Optics, Shanxi University, Taiyuan, Shanxi, 030006, P.R. China

X. Zhang, Prof. Y. Li, Prof. J. Tang
Institute of Functional Nano & Soft Materials, Soochow University, Suzhou 215123, P. R. China

X. He, Prof. J. Chen, Prof. J. Xu
State Key Laboratory of Precision Spectroscopy, Zhongshan Campus, East China Normal University, 200062, Shanghai, P. R. China

Dr. X. Liu, Dr. S. Braun, Prof. Q. Bao, Prof. M. Fahlman
Department of Physics, Chemistry and Biology, IFM, Linköping University SE-58183 Linköping, Sweden

X. Zheng, Prof. Y. Jin
Centre for Chemistry of High-Performance & Novel Materials, State Key Laboratory of Silicon Material, Department of Chemistry, Zhejiang University, 310027, Hangzhou, P. R. China

Keywords: triple-cation mixed halide perovskite, thermal-induced degradation, stability, efficiency, perovskite solar cell

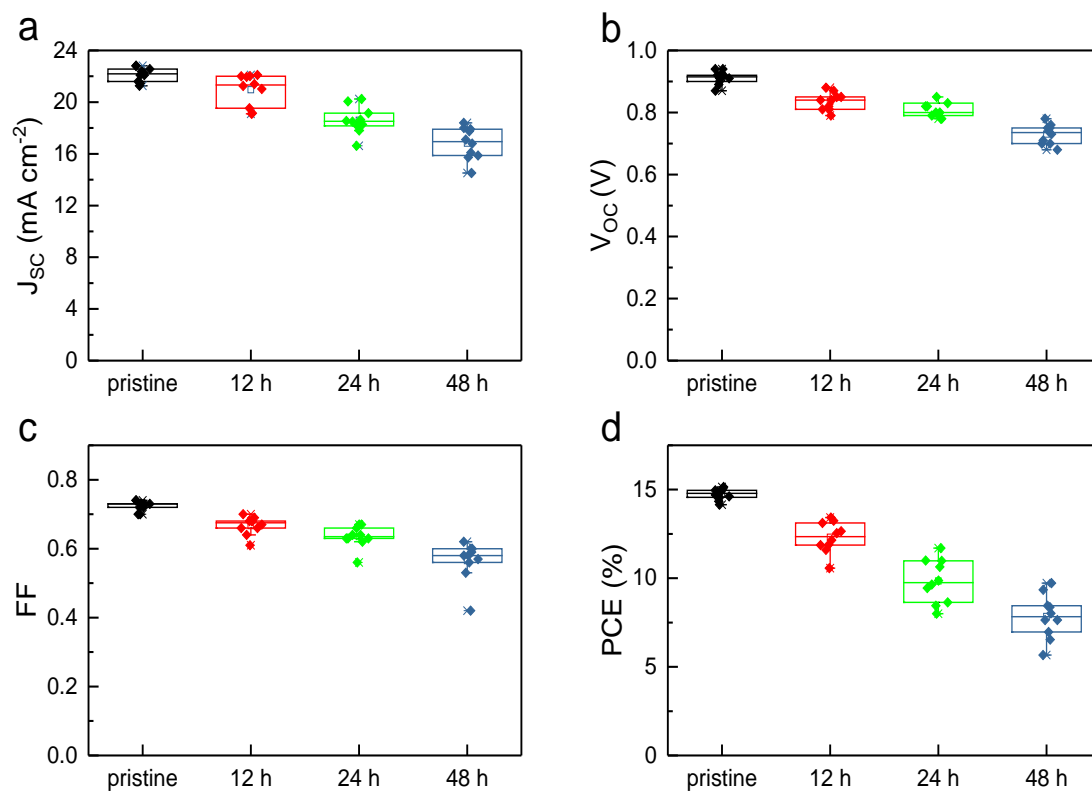


Figure S1. Statistical data for (a) J_{sc} , (b) V_{oc} , (c) FF and (d) PCE of the perovskite solar cells employing the perovskite layers annealed for various durations.

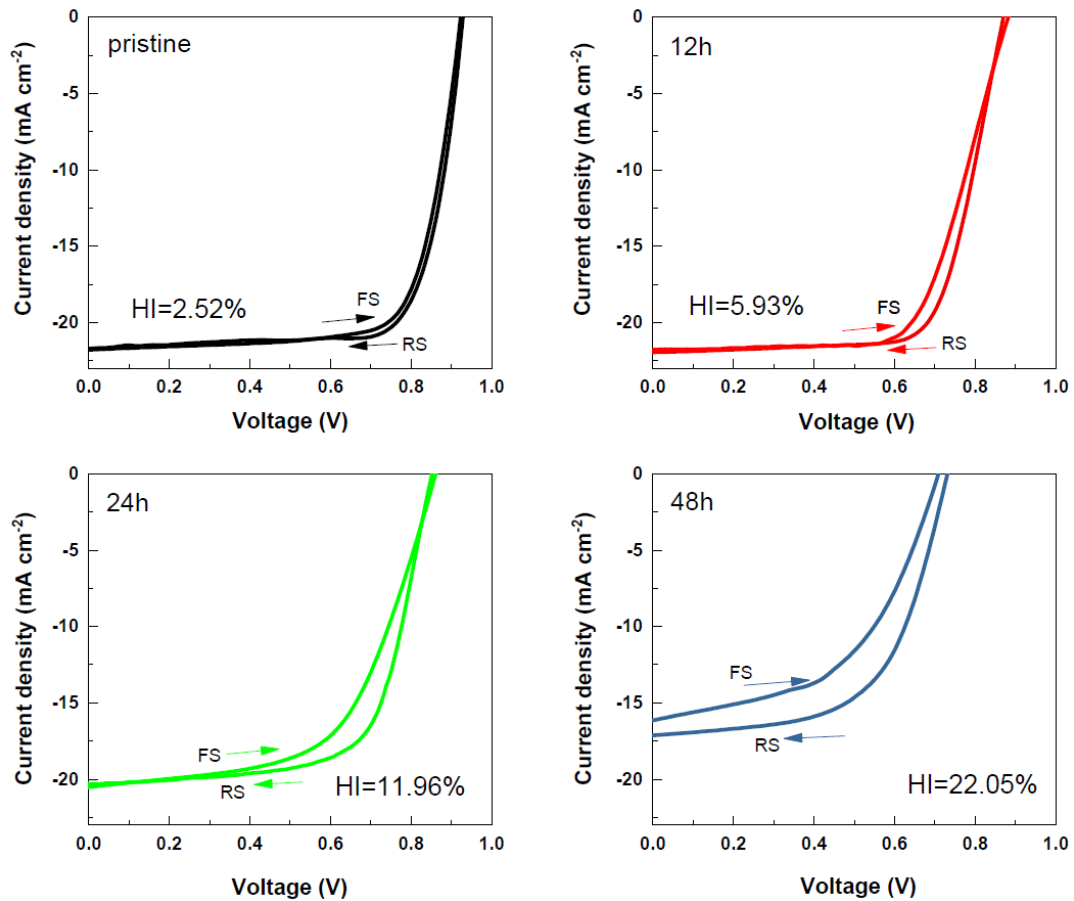


Figure S2. J-V curves from reverse scan (RS) and forward scan (FS) for the devices employing perovskite layers annealed for different durations. We use hysteresis index (HI) to estimate the hysteresis effect: $HI = (PCE_{reverse} - PCE_{forward}) / PCE_{reverse}$. $PCE_{reverse}$ and $PCE_{forward}$ are power conversion efficiency from reverse and forward scan, respectively.

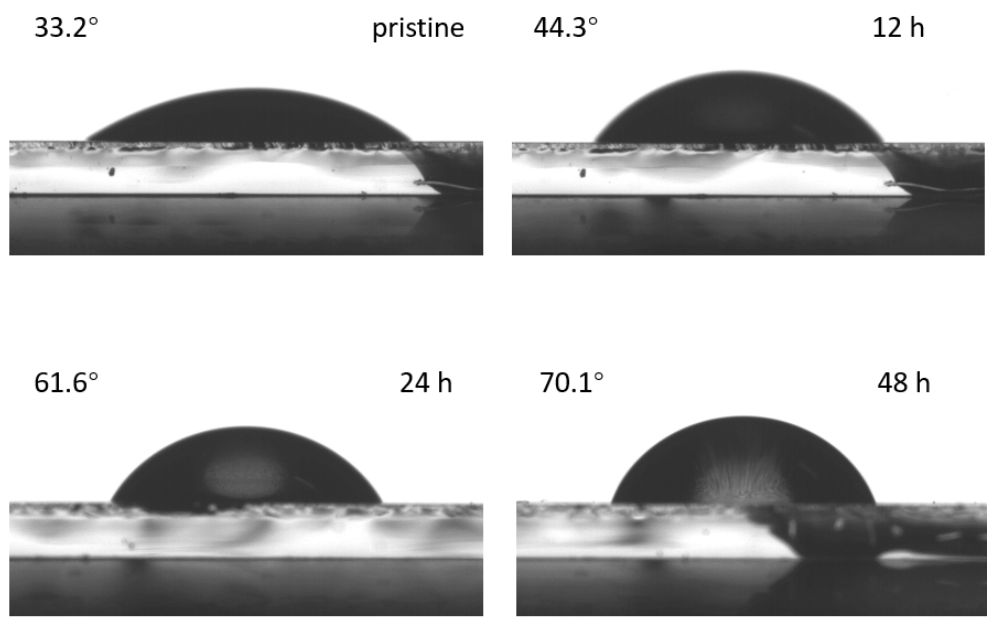


Figure S3. Water contact angle of perovskite layers annealed for various durations.

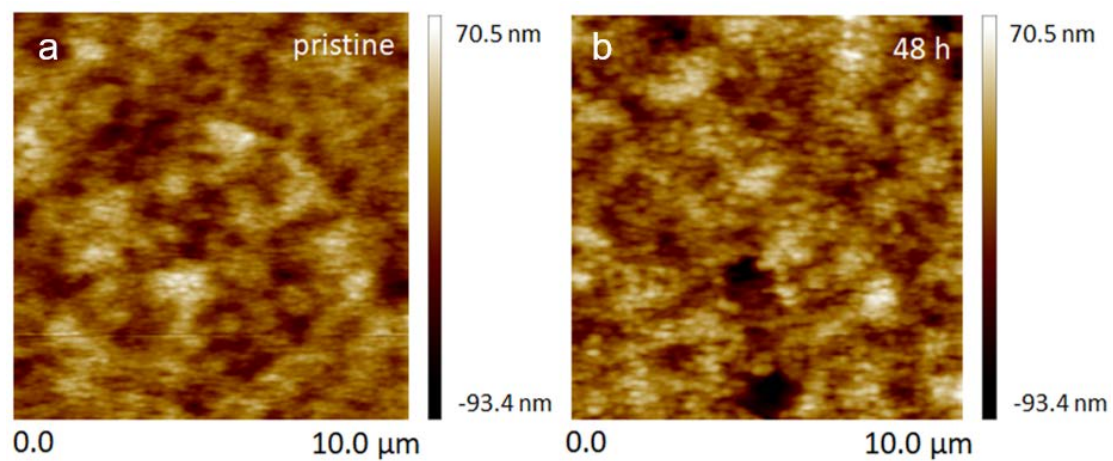


Figure S4. AFM topography images of (a) pristine and (b) annealed perovskite films for 48 h.

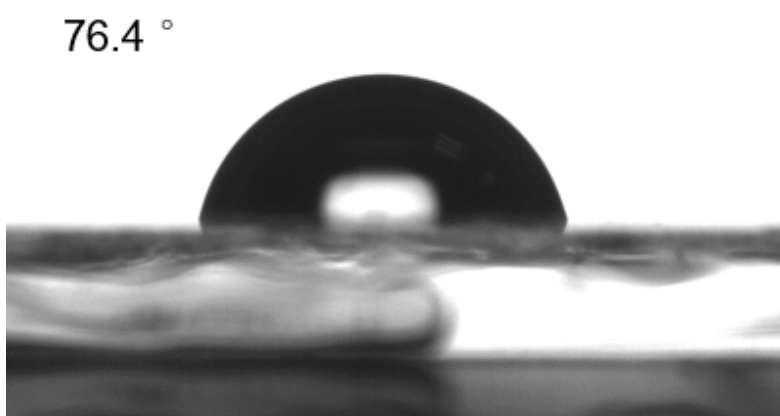


Figure S5. Water contact angle of the PbI₂ film

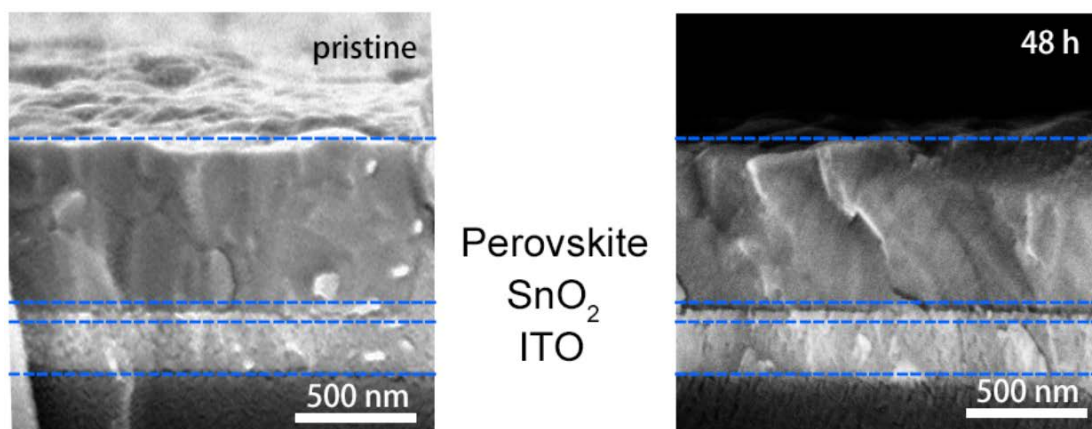


Figure S6. Cross-sectional SEM images of ITO/SnO₂/perovskite employing pristine and annealed perovskite films for 48 h.

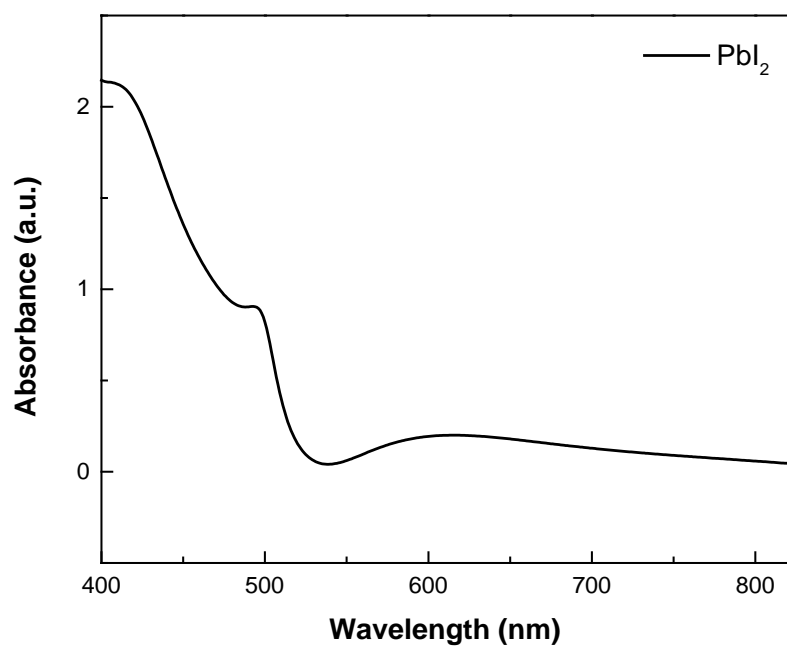


Figure S7. Absorption spectra of the PbI₂ film.

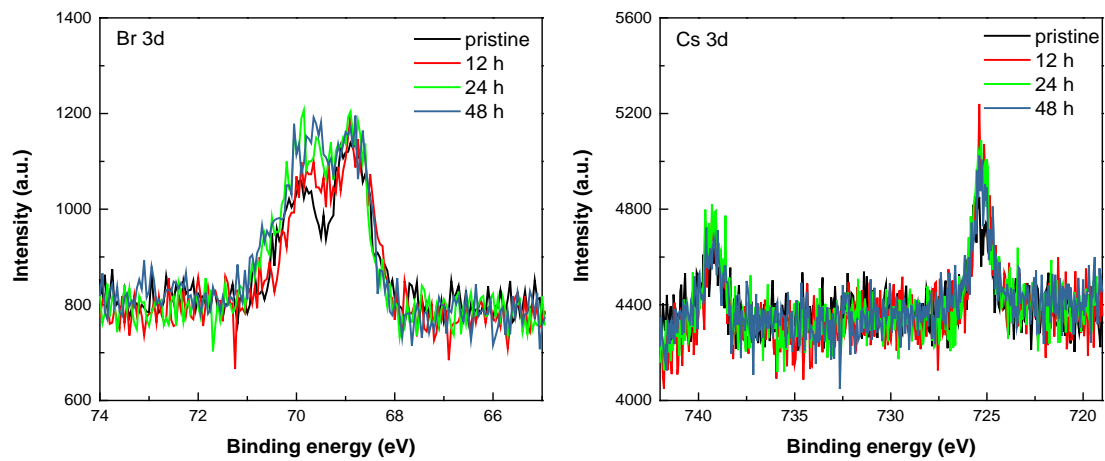


Figure S8. XPS core level evolution of Br 3d and Cs 3d of the pristine and annealed perovskite films with different times

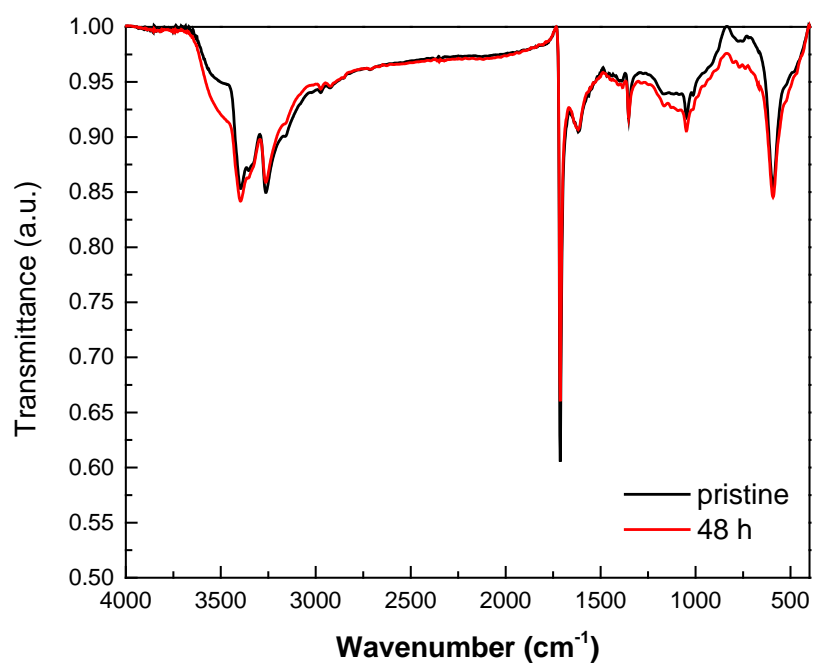


Figure S9. FTIR spectra of the perovskite film before and after annealing for 48 h.

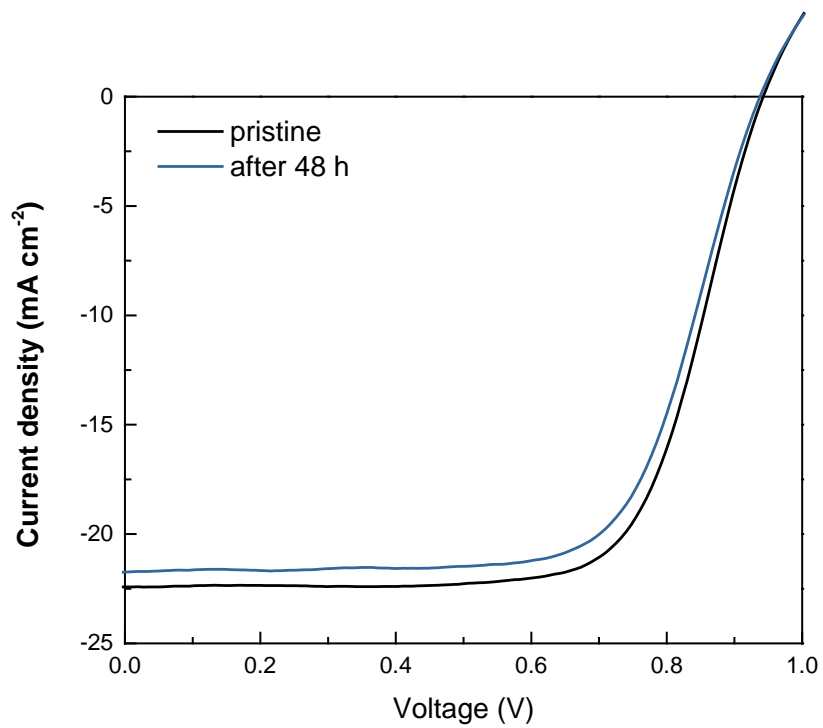


Figure S10. J-V curve change of ITO/PEDOT:PSS/pristine perovskite /PCBM/Ag stored in N₂ filled glove box for 48 h.

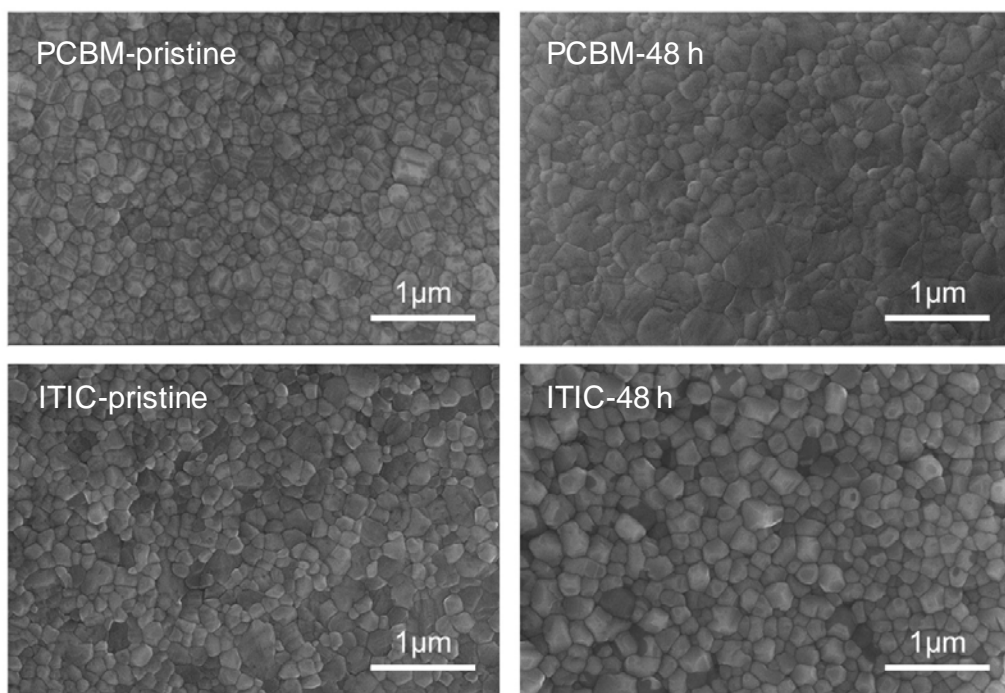


Figure S11. Top-view SEM images of PCBM and ITIC passivated perovskite films before and after 48 h annealing under 85 °C. There is no clear change before and after annealing.

Table S1. Summary of the trap densities and hole mobility of the pristine and annealed perovskite films for various durations.

	pristine	12 h	24 h	48 h
V_{TFL} (V)	1.99	2.60	2.70	2.93
N_{traps} (cm^{-3})	2.05×10^{16}	2.68×10^{16}	2.78×10^{16}	3.02×10^{16}
μ_{h} ($\text{cm}^2 \text{ V}^{-1} \text{ S}^{-1}$)	0.15	0.14	8.64×10^{-2}	3.19×10^{-2}

Table S2. TRPL characterizations of the pristine and annealed perovskite films for various durations.

	pristine	12 h	24 h	48 h
τ_1 (ns)	30.95	19.65	7.87	7.05
τ_2 (ns)	128.64	156.20	94.50	83.38
τ_{average} (ns)	115.61	147.50	88.85	78.82